

1

2

3

4

5

6

7

8

9

10

11

12

13

14

15

16

17

18

19

**A new method to retrieve the diurnal variability of planetary
boundary layer height from lidar under different thermodynamic
stability conditions**

Tianning Su¹, Zhanqing Li^{1,2*}, Ralph Kahn³

¹Department of Atmospheric and Oceanic Science & ESSIC, University of Maryland,
College Park, Maryland 20740, USA

²State Key Laboratory of Remote Sensing Science and College of Global Change and
Earth System Science, Beijing Normal University, 100875, Beijing, China

³Climate and Radiation Laboratory, Earth Science Division, NASA Goddard Space
Flight Center, Greenbelt, MD, USA

** Correspondence to: Zhanqing Li (zhanqing@umd.edu)*

Abstract

20
21 The planetary boundary layer height (PBLH) is an important parameter for
22 understanding the accumulation of pollutants and the dynamics of the lower
23 atmosphere. Lidar has been used for tracking the evolution of PBLH by using aerosol
24 backscatter as a tracer, assuming aerosol is generally well-mixed in the PBL; however,
25 the validity of this assumption actually varies with atmospheric stability. This is
26 demonstrated here for stable boundary layers (SBL), neutral boundary layers (NBL),
27 and convective boundary layers (CBL) using an 8-year dataset of micropulse lidar
28 (MPL) and radiosonde (RS) measurements at the ARM Southern Great Plains, and
29 MPL at the GSFC site. Due to weak thermal convection and complex aerosol
30 stratification, traditional gradient and wavelet methods can have difficulty capturing
31 the diurnal PBLH variations in the morning and forenoon, as well as under stable
32 conditions generally. A new method is developed that combines lidar-measured
33 aerosol backscatter with a stability dependent model of PBLH temporal variation
34 (DTDS). The latter helps “recalibrate” the PBLH in the presence of a residual aerosol
35 layer that does not change in harmony with PBL diurnal variation. The hybrid method
36 offers significantly improved PBLH detection, with better correlation and smaller
37 biases, under most thermodynamic conditions, especially for SBL and CBL. Relying
38 on the physical process of PBL diurnal development, different schemes are developed
39 for growing, maintenance, and decaying periods. Comprehensive evaluation of this
40 new method shows much better tracking of diurnal PBLH variation and significantly
41 smaller biases under various pollution levels.

42 1. Introduction

43 The planetary boundary layer (PBL) is the lowest layer of the atmosphere, and
44 tends to be relatively well-mixed (Garratt, 1994; Kaimal and Finnigan, 1994). It plays
45 a dominant role in the surface-atmosphere exchanges of heat, moisture, momentum,
46 gases, and pollutants (Caughey, 1984; Holtslag and Nieuwstadt, 1986; Mahrt, 1999).
47 The PBL height (PBLH) is a meteorological variable that strongly affects the vertical
48 extent of near-surface transport and dispersion processes, and is a key parameter in
49 weather and climate modeling (Haeffelin et al. 2012; Seibert et al. 2000). As PBLH
50 determines the volume available for near-surface pollutant dispersion, it is a crucial
51 variable for monitoring and simulating surface pollutant behaviors (Gan et al. 2011;
52 Monks et al. 2009; Su et al. 2018). Thermodynamic stability is a key variable of the
53 PBL; it influences convection, precipitation, and turbulence (Emanuel 1994; Guo et al.
54 2017; Lilly 1968; Matsui et al. 2004; Lou et al., 2019). Based on the thermodynamic
55 stability in the lower atmosphere, the PBL can be classified into three dominant types:
56 stable boundary layers (SBL), neutral boundary layers (NBL), and convective
57 boundary layers (CBL) (Caughey and Palmer 1979; Garratt 1994; Liu and Liang
58 2010).

59 Multiple approaches have been developed to determine the PBLH based on
60 observations, including *in situ* radiosonde (Stull 1988) and remote sensing (Menut et
61 al. 1999) methods, as well as parameterizations based on laboratory experiments (Park
62 et al. 2001). The most common approach for deriving PBLH is from radiosonde
63 measurements (RS) of temperature, humidity, and/or wind profiles as a function of

64 pressure (Angevine et al. 1994; Guo et al. 2016; Liu and Liang 2010; Seidel et al.
65 2010; Zhang et al. 2018). Although RS is the traditional and standard method for
66 determining PBLH, it has very limited coverage in both space and time. Regular RS
67 launches occur routinely twice a day from a fixed set of meteorological stations, and
68 thus cannot capture well the diurnal or spatial PBLH variations. Ground-based lidar,
69 such as micropulse lidar (MPL), measures aerosol backscatter with high resolution in
70 temporal and vertical scales, and has also been widely used to derive PBLH. (Eresmaa
71 et al. 2006; Hageli et al. 2000; Liu et al. 2018; Luo et al. 2014; Sawyer and Li 2013;
72 Su et al. 2017a; Tucker et al. 2009; Yang et al. 2013; Chu et al. 2019; Welton et al.
73 2000). Although the spatial coverage is still limited, several projects led by NASA and
74 the Department of Energy offer ample MPL measurements, such as MPLNET,
75 Atmospheric Radiation Measurement, DISCOVER-AQ, etc. (Campbell et al., 2002;
76 Welton et al. 2001, 2002; Lewis et al. 2013; Crawford and Pickering. 2014).
77 Numerous methods have been proposed to retrieve the PBLH from lidar, ranging from
78 visual inspection (Boers et al. 1984), to setting a signal threshold (Melfi et al. 1985),
79 wavelet transform (Cohn and Angevine 2000; Davis et al. 2000), fitting to idealized
80 profile (Steyn et al. 1999), changes in depolarization ratio (Bravo-Aranda et al. 2017),
81 identifying maximum signal variance (Hooper and Eloranta 1986; Su et al. 2017b;
82 Zhang et al. 2016), and first (Flamant et al. 1997), logarithmic (Summa et al. 2013),
83 normalized (He et al. 2006), and cubic root gradient methods (Yang et al. 2017), as
84 well as the combination of the wavelet technique and image processing (Lewis et al.
85 2013).

86 Although numerous algorithms have been applied to long-term PBL
87 measurements, and have been validated at multiple sites over the world, most PBLH
88 algorithms are designed for CBL conditions (e.g. Li et al. 2017a; Poltera et al. 2017).
89 The afternoon PBL is typically considered convective, with a peak at ~15:00 local
90 time; in contrast SBL generally dominates at night (Nieuwstadt 1984; Poulos et al.
91 2002). In addition, SBLs and NBLs can form under certain meteorological conditions
92 during the day as well, and can occur even in the afternoon (Medeiros et al. 2005;
93 Poulos et al. 2002; Stull 1988; Zhang et al. 2018). Evaluation of these algorithms for
94 SBLs has been limited, and in particular, evaluation of lidar-based PBL detection
95 under the full range of atmospheric stability conditions is still lacking.

96 As such, the current study presents a new method to retrieve PBL variability from
97 MPL under Different Thermo-Dynamic Stabilities (namely, the DTDS algorithm).
98 The thermodynamic stability is represented by the near-surface potential temperature
99 profile in the context of the boundary layer vertical structure. Long-term MPL
100 measurements from 2010 to 2018, acquired at the Department of Energy's
101 Atmospheric Radiation Measurement Southern Great Plains (ARM SGP) site, are
102 used for validation. PBLH retrievals derived from the DTDS are compared with the
103 commonly used gradient and wavelet methods, and are explicitly compared against
104 RS results under SBL, NBL, and CBL conditions. The performance of PBLH derived
105 from MPL under different aerosol loadings is also considered.

106 This paper proceeds as follows: Section 2 describes the study sites and MPL
107 system. Section 3 describes the method in terms of its physical principles,

108 implementation, and determination of the thresholds required by the DTDS method.
109 Evaluation is presented in section 4, and a brief discussion and conclusion are given in
110 Section 5.

111

112 **2. Description of the site and instruments**

113 *2.1. Radiosonde*

114 RS launches took place at least four times per day at the SGP site near Ponca City,
115 Oklahoma (36°36' N, 97°29' W), usually at 00:30, 6:30, 12:30, and 18:30 local time
116 (LT). To avoid inconsistency between summer and winter, daylight saving time
117 (summer time) is used consistently for local time throughout the year. Besides the
118 routine measurements at these fixed times, there are fewer, but still considerable,
119 numbers of RS measurements acquired at other times of day, especially during special
120 field experiments. Supplemental RS sampling at 0930, 1200, 1300, 1530, 1900 LT
121 were acquired for around 4% of the total cases. In this study, we only utilize the RS
122 data during 06:30-19:00 LT. RS vertical resolution varies according to the balloon
123 ascent rate, but data points occur approximately 10 m apart. We resample the
124 radiosonde data using linear interpolation to achieve a vertical resolution of 5-hPa.

125 We use a well-established method developed by Liu and Liang. (2010) to retrieve
126 the PBLH based on the gradient profile of potential temperature. Here, we focus only
127 on PBL driven by buoyancy, and hence, low-level jet conditions are excluded, based
128 on radiosonde wind profiles (Liu and Liang 2010; Miao et al. 2018). Furthermore, the
129 PBLH can be classified as SBL, NBL, or CBL based on the thermodynamic stability

130 conditions. PBL types are determined by calculating the near-surface potential
131 temperature difference (PTD) between the lowest fifth and second layers above the
132 surface (i.e., an interval of 5-hPa). Specifically, if the PTD is higher than 0.1 K and
133 the bulk Richardson number in the lowest 0.1km is positive, the PBL is identified as
134 SBL; if the PTD is between -0.1 K and 0.1 K, the PBL is identified as NBL; other
135 PBL cases are considered CBL (Tokinaga et al. 2006; Zhang et al. 2018).

136

137 *2.2. Micropulse lidar system*

138 This study uses an MPL backscatter time series collected at the SGP site (36°36'
139 N, 97°29' W). The dataset spans June 2010 through June 2018 with high continuity
140 (Campbell et al. 2002). The MPL observed at 532 nm wavelength with both parallel
141 and perpendicular polarization. The backscatter profiles have a vertical resolution of
142 15 m and a temporal resolution of 10 s. Due to incomplete laser pulses, there is a 150
143 m near-surface “blind zone”. As standard processes, background subtraction,
144 saturation, overlap, after-pulse, and range corrections are applied to the raw MPL data
145 to derive the normalized signal (NS) (Campbell et al. 2002; Campbell et al. 2003; Yan
146 et al. 2014). There are quality-control flags along with the MPL measurements.
147 Erroneous data and rainy cases are eliminated from our analysis. We supplement these
148 data with the MPL observations at the GSFC site (38 °59' N, 76°50' W) from
149 MPLNET, following similar data processing procedure (Welton et al. 2001, 2002). We
150 also collect RS data at a nearby NOAA station (USM00072403, 38 °59' N, 77°29' W)
151 to match with MPL data at GSFC. MPL data and RS measurements during morning

152 (0800LT) and afternoon are both available on 80 days between 2002 and 2016.

153 Hereafter, “afternoon” refers to the period from 1200 to 1830 LT.

154

155 **3. Development of the DTDS**

156 *3.1. A brief overview of existing algorithms*

157 Numerous methods have been proposed to retrieve the PBLH from backscatter
158 lidar. These methods rely on the principle that a temperature inversion often exists at
159 the top of the PBL, trapping moisture and aerosols (Seibert et al. 2000), which causes
160 a sharp decrease in the aerosol backscatter signal from the PBL upper boundary to
161 free troposphere. Traditionally, the methods fall into two categories: (i) gradient-based
162 algorithms that track gradients in the vertical distribution of aerosols (i.e., gradients of
163 the backscatter profiles (Flamant et al. 1997; He et al. 2006; Sicard et al. 2006;
164 Summa et al. 2013; Yang et al. 2017), and (ii) wavelet transform algorithms that track
165 the covariance transform of the Haar function (Baars et al. 2008; Brooks 2003; Cohn
166 and Angevine 2000; Davis et al. 2000). The merits and limitations of these approaches
167 were evaluated by Sawyer and Li (2013), who proposed a joint approach that takes
168 advantage of the two, and can be applied to any type of measurements, including RS
169 and lidar, and compared their performance.

170 In this paper, we compare the performance of the DTDS with the traditional
171 algorithms over the diurnal range of stability conditions. The gradient method is
172 adapted from Amiridis et al. (2007) and Flamant et al. (1997), and we set the first
173 derivative of lidar backscatter signals as the gradient profile. The wavelet method is

174 another commonly used, though more sophisticated, method. As a way of detecting
 175 step changes, the wavelet method was introduced by Gamage and Hagelberg (1993).

176 The Haar wavelet can be defined as

$$177 \quad h\left(\frac{z-b}{a}\right) = \begin{cases} +1: & b - \frac{a}{2} \leq z < b \\ -1: & b < z \leq b + \frac{a}{2} \\ 0: & \text{elsewhere} \end{cases} \quad (1)$$

178 where z is altitude, b translates the location where the function is centered, and a is
 179 called the “dilation” of the function. Then, the covariance transform of the Haar
 180 function $W_f(a, b)$ is defined as

$$181 \quad W_f(a, b) = \frac{1}{a} \int_{z_b}^{z_t} f(z) h\left(\frac{z-b}{a}\right) dz \quad (2)$$

182 where $f(z)$ is the lidar backscatter signal and z_t/z_b indicates the lower/upper limits
 183 of the profile, respectively. The value b at which $W_f(a, b)$ reaches its maximum
 184 value with a coherent scale of a is usually considered as the PBLH (Brooks 2003). In
 185 this study, we select the dilation a as 400m, which is consistent with previous studies
 186 (Compton et al. 2013; Davis et al. 2000).

187 In Fig. 1, we compare the PBLH derived from MPL using these two methods with
 188 RS results, for different local times (LT). There is generally much better agreement
 189 between MPL-PBLH and RS-PBLH at 1230 and 1830 LT than at 0630. This is clearly
 190 denoted by the distinct differences, factors of 3-4, in their linear correlation
 191 coefficients. The very poor agreement for morning cases is associated with the fact
 192 that the PBL is not well developed, as indicated by the existence of a strong surface

193 inversion and residual layers. All these factors complicate PBLH identification. As
194 such, these MPL methods fail in identifying the PBLH under the SBL conditions that
195 tend to dominate in the morning.

196 Despite the dominance of the CBL in the afternoon, SBL and NBL can also occur
197 under some meteorological conditions. Based on the RS data from SGP, SBL
198 dominates during the morning (0630LT), and its occurrence frequency is more than 90%
199 in the dataset used for the current study. In the noontime (1230LT), the occurrence
200 frequency of CBL is only ~3%, followed by 43% for NBL, and 54% for SBL. In the
201 late afternoon (1830LT), the SBL frequency is about 38%, followed by 47% for NBL,
202 and 15% for CBL. Fig. 2 shows a comparison of afternoon PBLH derived from MPL
203 and RS under SBL, NBL, and CBL conditions. In the afternoon (1200-1830 LT), SBL,
204 NBL and CBL conditions occur for 19%, 45%, and 36% of total cases in our dataset.
205 Again, MPL-PBLH shows much better agreement with RS-PBLH for CBL and NBL
206 conditions than for SBL, especially where $RS-PBLH < 1.0$ km. Therefore, MPL has a
207 major problem retrieving PBLH for weak convective as well as SBL cases. Note also
208 that for all three PBL types, root-mean-square error (RMSE) values are around 0.6
209 km.

210

211 *3.2. Description of the DTDS*

212 In order to overcome problems with SBL conditions, we develop a new approach
213 for retrieving MPL-PBLH that performs better and more uniformly under all
214 thermodynamic stability conditions. The physical basis of our DTDS method is to

215 account for both the vertical coherence and temporal continuity of the PBLH. Given
216 that the aerosol within the boundary layer is usually well mixed, a distinct step due to
217 aerosol is sought in the backscatter signal as the top of a PBL layer, which follows the
218 gradient and wavelet transform methods. The development of the PBL can be divided
219 into three phases: growing, decaying, and “other” (i.e., maintenance), and different
220 selection schemes can be applied to these different phases. A schematic diagram of the
221 DTDS is presented in Fig. 3, and the procedures are detailed below.

222 First, the MPL backscatter profiles are averaged over 10-minute intervals. Then,
223 we identify the local maximum positions (LMPs) (range: 0.25-4km) in the covariance
224 transform function collocated with a signal gradient larger than a certain threshold.
225 The threshold values are discussed in Section 3.3. The aerosol vertical structure can
226 be represented by multiple LMPs. Each LMP is the potential position of PBLH.

227 $H(i)$ represents the retrieved PBLH for time i . For the starting point (0700 LT),
228 the PBLH ($H(0)$) is given by the morning RS launched at 0630 LT (or the lowest
229 LMP if RS is not available), after which we select the closest LMP at 0710 to $H(0)$
230 as $H(1)$. If we find a suitable $H(1)$, we identify the closest LMP at the next timestep
231 as $H(2)$. Generally, for time $i+1$, we select the closest LMP to $H(i)$ as $H(i+1)$.
232 The maximum variation rate (Max) is set to 0.2km, so the difference between $H(i+1)$
233 and $H(i)$ needs to be smaller than Max . Otherwise, $H(i+1)$ is set to equal to
234 $H(i)$, and is called a “quasi retrieval”. If we obtain two consecutive quasi retrievals,
235 $H(i)$ and $H(i+1)$, we set $H(i+1)$ to the lowest LMP in time $i+1$, and then,
236 determine $H(i+2)$ using above mentioned algorithms.

237 As shown in Fig. 3b, the selection scheme is different for the growing (0830-1400)
238 and decaying (1630-1900) PBL phases, defined by these pre-selected local time
239 periods. Due to surface heating by solar radiance, the PBLH tends to rise quickly
240 during the growing period, and generally reaches its daily maximum monotonically.
241 For time $i+1$, if we find two LMPs adjacent to the previous $H(i)$, we preferentially
242 select the one higher than $H(i)$ as $H(i+1)$ during this period. However, we
243 preferentially select the one lower than $H(i)$ as $H(i+1)$ during the decaying
244 period. Details of the selection scheme for different periods are shown in the Fig. 3b.
245 Generally, during the growing phase, we favor the nearest LMP above $H(i)$ as $H(i+1)$.
246 However, if the two nearest LMPs during the growing phase are above and below $H(i)$
247 and the upper LMP is twice as far from $H(i)$ as the lower, we will still select the lower
248 one as $H(i+1)$. We implement a similar selection scheme for decay phase, but in just
249 the opposite sense to that of grow phase. If we cannot find two LMPs adjacent to $H(i)$,
250 the potential PBLH position is selected as the nearest LMP.

251 A restart mechanism is also included in this algorithm, controlled by the
252 parameter “ Re ,” which remains at 0 as long as the selection scheme in Fig. 3b is
253 successful. For two contiguous times (i and $i+1$), if we cannot find the suitable $H(i)$
254 and $H(i+1)$, Re becomes larger than 1, and the algorithm “restarts.” Specifically,
255 the lowest LMP at time $i+2$ is selected as $H(i+2)$, and the iterative process is
256 restarted from there.

257 Cloud inevitably causes a step signal in the lidar backscatter, and thus, affects the
258 PBLH retrievals. Depending on type, clouds can interfere with PBLH retrievals,

259 though boundary layer top clouds can also be regarded as defining the PBLH. During
260 the development of the PBLH over land, fair-weather cumulus are often generated
261 from convection and high-humidity located at the top of PBL. Following the threshold
262 method, cloud or aerosol layers can be detected based on the gradient of
263 range-corrected signals (Dupont et al. 2011; Platt et al. 1994). Cloud can be further
264 distinguished based on the values of T and D for a certain layer, where T represents
265 the ratio of the peak signal to that of the layer base and D represents the maximum
266 negative slope within this layer. When $T > 3$ or $D < -7$, the layers are classified as clouds
267 (Wang and Sassen, 2001; Zhao et al., 2016). All low-level clouds below 4km are
268 identified, and then, we label these clouds as “boundary layer clouds” if their tops
269 coincide with the previous PBLH value retrieved under cloud-free conditions to
270 within 0.35 km. Due to the frequent occurrence of convection, we only identify
271 boundary layer clouds during the growing and maintenance periods. Other low-level
272 cloudy cases are excluded from the analysis.

273 *3.3. Sensitivity test of thresholds*

274 The detection of LMPs is a crucial part of the DTDS, and an appropriate threshold
275 is needed to identify step signals in the gradient profiles. The method is quite sensitive
276 to the threshold selection. A low threshold value will lead to too many LMPs, which
277 complicates PBLH identification, whereas too high a threshold value will constrain
278 the LMP selection, which could filter out the actual PBLH. Therefore, we conducted a
279 sensitivity test to select the threshold.

280 In many studies, the threshold for detecting step signals in PBL lidar profiles is set

281 to a constant value (Hageli et al. 2000; Yang et al. 2013). Instead, we apply a dynamic
282 threshold, which is associated with the noise level. In particular, we estimate the shot
283 noise (σ) induced by background light and dark currents in each profile (Welton et al.
284 2002; Liu et al. 2006; Whiteman et al. 2006). To exclude noise effects, the gradient
285 signal must be larger than the shot noise. The thresholds are set between σ and
286 4.5σ .

287 In Fig. 4, we present the correlation coefficient and RMSE values comparing the
288 DTDS-derived and RS-derived PBLH based on different thresholds. For these data,
289 we find that both the correlation coefficients and RMSE values achieve best
290 performance when the threshold is set as 3σ . A threshold value of 3σ is thus used in
291 the DTDS for detecting LMPs.

292

293 **4. Evaluation of the DTDS**

294 *4.1. Case study of the DTDS*

295 By using DTDS, we can continuously retrieve the daily PBLH during 0700-1900.
296 Fig. 5 illustrates three typical cases of backscatter profiles and PBLH retrievals under
297 different stability conditions on 25 Dec. 2014, 13 Sep. 2010, and 1 Jul. 2010,
298 respectively. Relatively complex aerosol stratification is indicated by multiple LMPs
299 for each profile, especially during the morning periods.

300 For the SBL case, clear aerosol stratification structure is shown, with little diurnal
301 variation. Due to relatively weak convection, the PBL does not develop well during
302 the entire day. However, there are multiple LMPs at different elevations (e.g. aerosol

303 step signals around 0.4km, 0.6km, and 1km). If we retrieve PBLH based on single
304 profiles, the retrievals would jump between different atmospheric layers, and would
305 not provide accurate results. With initial RS input in the morning, we coherently track
306 the PBLH by the DTDS during the entire day, and the result agrees well with
307 subsequent RS measurements.

308 For the NBL and CBL cases, the PBLH grows continuously from the initial points
309 constrained by RS measurements, and reach maxima around 1500LT. The retrievals
310 derived from the DTDS exclude interference from the complex aerosol structures that
311 occur in the morning. The PBLH generally maintains its highest value during
312 1500-1900LT for this case. Nonetheless, the PBLH starts to decay after 1600LT for
313 NBL. The selection scheme for the decaying period assures that our method can
314 distinguish the actual PBL from the aerosol residual layer. Moreover, boundary layer
315 clouds are identified for the NBL and CBL cases, and the retrieved PBLH location
316 remains consistent with the values under cloud-free conditions.

317 In general, DTDS reliably tracks the true PBLH development during daytime for
318 these three typical cases, and matches well the RS measurements. In some periods,
319 multiple gradients are found in the lidar backscatter observations. Despite complex
320 aerosol structure, the DTDS successfully identifies the diurnal variation of the PBLH
321 in each case, given the initial point constraint provided by the radiosonde data.

322

323 *4.2. Comparison between PBLHs derived from the DTDS and radiosonde*

324 We further apply DTDS to the 8-year MPL dataset at the ARM SGP site, and

325 compare the PBLH results with those from RS measurements. We prefer to use the
326 morning RS to constrain the initial position of PBLH. However, DTDS can still
327 perform without morning RS input. Figs 6a-c show comparisons between RS PBLH
328 and PBLH derived from the DTDS without RS constraints, under different
329 thermodynamic stability conditions during afternoon. Figs 6d-f show comparisons
330 between RS PBLH and PBLH derived from DTDS with RS constraints.

331 Compared to the gradient and wavelet methods (Fig. 2), the correlation
332 coefficients between PBLH derived from the DTDS and RS are higher for all PBL
333 types, and are improved especially for the SBL cases. Although the correlation is still
334 relatively weak for weakly convective cases, it is substantially improved relative to
335 the gradient and wavelet methods. Moreover, compared to the RMSE for the gradient
336 and wavelet methods, the RMSE values for the DTDS vs. RS are considerably
337 reduced under SBL and CBL conditions. Although DTDS is valid without the
338 morning RS input, better performance is achieved after assimilating morning RS input,
339 especially under SBL and CBL conditions. Due to the availability of RS, we analyze
340 the PBLH retrievals derived from the DTDS with the morning RS constraint in the
341 following sections.

342 In general, the PBLH retrievals derived from DTDS are improved for all PBL
343 types. Although the correlation coefficients are generally higher only under SBL
344 conditions, the RMSE values are considerably reduced for both SBL and CBL in the
345 study dataset. We supplement the validation of our method using MPL data at the
346 MPLNET GSFC site, and compare the retrievals with RS-PBLH at nearby locations

347 during the afternoon. DTDS also shows reasonably good performance for the GSFC
348 site (Fig. 7). Nonetheless, due to insufficient afternoon RS data in this area, the
349 sampling number is significantly less than at the SGP site.

350

351 *4.3. Diurnal cycles*

352 Fig. 8 presents the diurnal behavior of PBLH under SBL, NBL, and CBL
353 conditions. Since the thermodynamic condition during noontime is critical to the daily
354 PBL development and evolution, the daily PBL types are determined from the RS
355 measurements during 1230 LT, which generally corresponds to the most unstable
356 period of a day. The diurnal cycles derived from the DTDS match well with RS results.
357 Specifically, CBL is usually associated with strong solar heating of the surface, and
358 the PBL tends to rise continuously due to upward convection around noontime, and to
359 reach its maximum height around 1500. For cases that remain stable by midday, the
360 PBL does not develop well during the entire day. NBL is neutrally stratified, so the
361 potential temperature is nearly constant within the PBL, and turbulence has
362 approximately equal intensity in all directions. The diurnal cycle for NBL is similar to
363 CBL, and shows smaller variation.

364 Broadly speaking, PBLHs derived from DTDS show similar diurnal cycles with
365 those from the gradient and wavelet methods, but with both smaller biases and
366 standard deviation errors. The gradient-wavelet method tends to overestimate the
367 PBLH for SBL, and the diurnal cycle fluctuates chaotically under these conditions,
368 which may be caused by the algorithm assigning the PBLH to different atmospheric

369 layers inconsistently. For CBL, the gradient-wavelet method slightly overestimates
370 PBLH in the morning and around sunset, and slightly underestimates PBLH during
371 midday, compared to DTDS. In term of mean values, the RS-PBLH at 1530 is
372 significantly higher than MPL-PBLH. As the RS data are acquired at 1530 only for ~3%
373 of total cases, sampling biases contribute significantly to the observed differences. If
374 we only use matched cases of RS-PBLH and MPL-PBLH at 1530, the difference in
375 the PBLH means is less than 0.1 km. For NBL, the diurnal cycles derived from the
376 DTDS and gradient-wavelet methods generally agree well with RS and with each
377 other.

378 The PBLH growth rate during transient periods is a key factor associated with
379 boundary layer turbulence and eddies, as well as aerosol dilution (Carson 1973;
380 Driedonks 1982; Martin et al. 1988). We show the distribution of PBLH growth rates
381 during 0700-1230 LT under different thermodynamic stability conditions derived from
382 different methods in Fig. 9. The growth rate is calculated as the average change of
383 PBLH per hour during this period. For the majority cases, the growth rates are
384 positive, as expected. Clearly, strong and positive buoyancy forcing under CBL
385 conditions contributes to the large PBLH growth rate, which is near zero under SBL
386 conditions. However, conventional lidar gradient and wavelet methods cannot capture
387 well such phenomena; the derived PBLH growth rates are similar, and show much
388 larger variations under different thermodynamic stability conditions. After
389 assimilating PBLH derived from morning radiosonde data, the PBLH growth rate can
390 be estimated by DTDS with better accuracy. The absolute basis in PBLH growth rate

391 between RS and the wavelet/gradient methods is around 0.06 km/h, but is reduced to
392 about 0.033 km/h between RS and the DTDS.

393

394 *4.4. The impact of buoyancy forcing and aerosol loading*

395 Because the retrieval of PBLH from lidar depends on the aerosol backscatter
396 signal and thermodynamic stability, we further examine the absolute differences
397 between the PBLH retrievals from lidar and RS for different aerosol loadings and
398 stability conditions. The buoyancy (B) determines convection and can be expressed as
399 (Wallace and Hobbs 2006):

$$400 \quad B = -g\Delta z \frac{1}{\theta} \frac{d\theta}{dz} \quad (3)$$

401 where z is the height of the air parcel and g is the acceleration of gravity near Earth's
402 surface. θ is the virtual potential temperature of the environment. The
403 lower-atmosphere buoyancy is calculated as the integral of buoyancy in the lowest 0.5
404 km.

405 We further use the near-surface aerosol extinction (at 0.2km) derived from lidar to
406 represent pollution levels. The method for retrieving aerosol extinction from MPL has
407 been well demonstrated in multiple studies (e.g. Fernald, 1984; Klett, 1985). Due to
408 the uncertainty of the extinction-to-backscatter ratio (so-called lidar ratio), we use the
409 aerosol optical depth from multifilter rotating shadow-band radiometer (MFRSR) to
410 calibrate the aerosol extinction profiles (Harrison et al. 1994; Sinha et al., 2013; Lee et
411 al. 2010). Fig. 10 presents the absolute bias of PBLHs between MPL and RS for
412 various buoyancy forcing and aerosol extinction values. Compared with the

413 gradient-wavelet methods, the DTDS absolute bias is reduced by about 30% at
414 various convection intensities and pollution levels. The shaded areas in Fig. 10
415 indicate standard deviations, which are also larger for the gradient-wavelet methods
416 than DTDS.

417 The increased lower-atmosphere buoyancy can facilitate the mixing of aerosol
418 and humidity in the PBL, and thus can considerably reduce the absolute biases
419 between PBLH derived from RS and MPL. Meanwhile, a boomerang shape that
420 appears in Fig. 10b indicates that relatively large differences between PBLH derived
421 from MPL and RS happen at both low and high aerosol extinction. This phenomenon
422 may be caused by the aerosol signal and/or thermal convection. As the detection of
423 PBLH from lidar depends on the contrast between near-surface aerosol layers and the
424 free troposphere, the step signal would be weak when aerosol loading is low, which
425 could produce relatively large PBLH retrieval biases. On the other hand, high surface
426 aerosol loading is typically associated with weak surface heating and thermal
427 convection, producing insufficient vertical mixing of pollutants, and could therefore
428 also cause relatively large biases for MPL retrievals.

429 For the gradient-wavelet methods, the relative absolute biases are strongly subject
430 to buoyancy forcing and aerosol loading values, and can be larger than 40% for strong
431 downward forcing and high near-surface extinction, which are also likely to occur
432 together. For DTDS, the contrast between different convection intensities and
433 extinction levels is smaller, and the absolute biases are significantly reduced
434 compared to the alternative retrieval algorithms.

435

436 **5. Discussion and Conclusions**

437 In this paper, the PBL height (PBLH) retrieved from lidar is investigated
438 systematically, under stable boundary layers (SBL), neutral boundary layers (NBL),
439 and convective boundary layers (CBL) conditions, using an 8-year dataset of
440 micropulse lidar (MPL) and radiosonde (RS) measurements acquired at the ARM
441 Southern Great Plains research site. We present a DTDS algorithm aimed at
442 accurately retrieving the PBLH under Different Thermo-Dynamic Stabilities. This
443 method combines traditional approaches based on the observed aerosol vertical
444 profiles with a stability-dependent model of PBLH temporal variation. Where possible,
445 the method is initialized with early morning RS data, though this is not a strict
446 requirement for DTDS to be applied. For the rest of the diurnal cycle, relative to the
447 PBLH derived from radiosonde that is usually considered as ground-truth, the DTDS
448 method performs better than the widely used gradient and wavelet methods both in
449 terms of the PBLH magnitude and its diurnal variation, especially under SBL
450 conditions.

451 The DTDS method aims to maximize the temporal continuity of the PBLH. It
452 applies schemes specific to the growing (0830-1400 local time (LT)), decaying
453 (1630-1900 LT) and maintenance periods for selecting successive PBLH values,
454 based on a physical model of PBL development. Although the actual PBLH diurnal
455 cycle is more complicated, this scheme is proven to work well for most cases studied.
456 The PBLH derived from DTDS is likely to increase during the growing phase and

457 decrease during the decaying phase, but the method can also identify it as declining
458 during the period of typical growth or increasing during the period of typical decay if
459 conditions warrant (e.g. Fig. 5a). Convective boundary layer clouds are identified to
460 diagnose the PBLH for cloudy cases. As the PBLH is often indeterminate from MPL
461 data alone in the morning, we tend to use the morning RS observations to constrain
462 the initial PBLH position for subsequent retrievals, although the method is still valid
463 without any RS data.

464 As a result, DTDS shows significantly improved performance in comparison to
465 the RS-based method, with the correlation coefficient improved by up to a factor of
466 3-4 under SBL conditions during afternoon, when the conventional methods often fail
467 due to the weak vertical mixing and complex aerosol stratification. RMSE is actually
468 reduced under all conditions, though improvement is most significant under SBL and
469 CBL conditions. The DTDS method can largely exclude interference from the
470 residual aerosol layer and other complex aerosol structures.

471 The PBLH derived from lidar is widely used to investigate air quality issues and
472 thermodynamic processes in the PBL (e.g. Beniston et al. 1990; Davies et al. 2007;
473 Geiss et al. 2017; Su et al. 2018; Tang et al. 2015). Although the lidar retrievals
474 exhibit satisfactory overall performance, the accuracy of lidar retrievals can vary
475 considerably under different stability conditions and aerosol levels, and thus, may
476 cause uncertainties in these studies. This problem is not completely solved, but our
477 method gives some insight into this issue by reducing biases under various stability
478 conditions and aerosol loadings.

479 Stable conditions are associated with downward forcing in the lower atmosphere,
480 and they exert important constraints on severe pollution episodes. Being able to detect
481 the PBLH under such conditions would help understand and model the development
482 of air pollution episodes, especially in the morning before the PBL is fully developed.
483 The method is also valuable for investigating PBL-aerosol interaction mechanisms
484 under various meteorological and thermodynamic stability conditions, which remains
485 an outstanding problem in studies concerning atmospheric environment (Li et al.
486 2017b). The PBLH derived using the DTDS approach may also be beneficial for
487 pollution control management, as it helps improve understanding of aerosol
488 dispersion.

489

490 **Acknowledgements**

491 We acknowledge the provision of radiosonde and MPL data by the U.S. Department
492 of Energy's ARM program (<https://www.archive.arm.gov/discovery>). We thank Dr. E.
493 J. Welton and his team for their efforts in establishing and maintaining the GSFC site.
494 We extend sincerest thanks to the MPLNET for their datasets. This work is supported
495 in part by grants from the National Science Foundation (AGS1837811 and
496 AGS1534670). The contributions of R. Kahn are supported in part by NASA's
497 Climate and Radiation Research and Analysis Program under H. Maring, and NASA's
498 Atmospheric Composition Modeling and Analysis Program under R. Eckman.

499

500 **References**

- 501 Amiridis, V., Melas, D., Balis, D.S., Papayannis, A., Founda, D., Katragkou, E., Giannakaki,
502 E., Mamouri, R.E., Gerasopoulos, E., & Zerefos, C. (2007). Aerosol lidar observations
503 and model calculations of the planetary boundary layer evolution over greece, during the
504 march 2006 total solar eclipse. *Atmospheric Chemistry and Physics*, 7, 6181-6189
- 505 Angevine, W.M., White, A.B., & Avery, S.K. (1994). Boundary-Layer Depth and Entrainment
506 Zone Characterization with a Boundary-Layer Profiler. *Boundary-Layer Meteorology*, 68,
507 375-385
- 508 Baars, H., Ansmann, A., Engelmann, R., & Althausen, D. (2008). Continuous monitoring of
509 the boundary-layer top with lidar. *Atmospheric Chemistry and Physics*, 8, 7281-7296
- 510 Beniston, M., Wolf, J.P., Benistonrebetz, M., Kolsch, H.J., Rairoux, P., & Woste, L. (1990).
511 Use of Lidar Measurements and Numerical-Models in Air-Pollution Research. *Journal of*
512 *Geophysical Research-Atmospheres*, 95, 9879-9894
- 513 Boers, R., Eloranta, E.W., & Coulter, R.L. (1984). Lidar Observations of Mixed Layer
514 Dynamics - Tests of Parameterized Entrainment Models of Mixed Layer Growth-Rate.
515 *Journal of Climate and Applied Meteorology*, 23, 247-266
- 516 Bravo-Aranda, J.A., Moreira, G.D., Navas-Guzman, F., Granados-Munoz, M.J.,
517 Guerrero-Rascado, J.L., Pozo-Vazquez, D., Arbizu-Barrena, C., Reyes, F.J.O., Mallet, M.,
518 & Arboledas, L.A. (2017). A new methodology for PBL height estimations based on lidar
519 depolarization measurements: analysis and comparison against MWR and WRF
520 model-based results. *Atmospheric Chemistry and Physics*, 17, 6839-6851
- 521 Brooks, I.M. (2003). Finding boundary layer top: Application of a wavelet covariance
522 transform to lidar backscatter profiles. *Journal of Atmospheric and Oceanic Technology*,
523 20, 1092-1105
- 524 Campbell, J.R., Hlavka, D.L., Welton, E.J., Flynn, C.J., Turner, D.D., Spinhirne, J.D., Scott,
525 V.S., & Hwang, I.H. (2002). Full-time, eye-safe cloud and aerosol lidar observation at
526 atmospheric radiation measurement program sites: Instruments and data processing.
527 *Journal of Atmospheric and Oceanic Technology*, 19, 431-442
- 528 Campbell, J.R., Welton, E.J., Spinhirne, J.D., Ji, Q., Tsay, S.C., Piketh, S.J., Barenbrug, M., &

529 Holben, B.N. (2003). Micropulse lidar observations of tropospheric aerosols over
530 northeastern South Africa during the ARREX and SAFARI 2000 dry season experiments.
531 *Journal of Geophysical Research-Atmospheres*, 108

532 Carson, D.J. (1973). The development of a dry inversion - capped convectively unstable
533 boundary layer. *Quarterly Journal of the Royal Meteorological Society*, 99, 450-467

534 Caughey, S.J., & Palmer, S.G. (1979). Some Aspects of Turbulence Structure through the
535 Depth of the Convective Boundary-Layer. *Quarterly Journal of the Royal Meteorological*
536 *Society*, 105, 811-827

537 Caughey, S.J. (1984). Observed characteristics of the atmospheric boundary layer. In
538 Atmospheric turbulence and air pollution modelling (pp. 107-158). Springer, Dordrecht.

539 Chu, Y., Li, J., Li, C., Tan, W., Su, T., & Li, J. (2019). Seasonal and diurnal variability of
540 planetary boundary layer height in Beijing: Intercomparison between MPL and WRF
541 results. *Atmospheric Research*, 227, 1-13.

542 Crawford, J. H., & Pickering, K. E. (2014). DISCOVER-AQ: Advancing strategies for air
543 quality observations in the next decade. *Environ. Manage*, 4-7.

544 Cohn, S.A., & Angevine, W.M. (2000). Boundary layer height and entrainment zone thickness
545 measured by lidars and wind-profiling radars. *Journal of Applied Meteorology*, 39,
546 1233-1247

547 Compton, J.C., Delgado, R., Berkoff, T.A., & Hoff, R.M. (2013). Determination of Planetary
548 Boundary Layer Height on Short Spatial and Temporal Scales: A Demonstration of the
549 Covariance Wavelet Transform in Ground-Based Wind Profiler and Lidar Measurements.
550 *Journal of Atmospheric and Oceanic Technology*, 30, 1566-1575

551 Davies, F., Middleton, D.R., & Bozier, K.E. (2007). Urban air pollution modelling and
552 measurements of boundary layer height. *Atmospheric Environment*, 41, 4040-4049

553 Davis, K.J., Gamage, N., Hagelberg, C.R., Kiemle, C., Lenschow, D.H., & Sullivan, P.P.
554 (2000). An objective method for deriving atmospheric structure from airborne lidar
555 observations. *Journal of Atmospheric and Oceanic Technology*, 17, 1455-1468

556 Driedonks, A.G.M. (1982). Models and Observations of the Growth of the Atmospheric
557 Boundary-Layer. *Boundary-Layer Meteorology*, 23, 283-306

558 Dupont, J.C., Haeffelin, M., Morille, Y., Comstock, J.M., Flynn, C., Long, C.N., Sivaraman,

559 C., & Newson, R.K. (2011). Cloud properties derived from two lidars over the ARM SGP
560 site. *Geophysical Research Letters*, 38

561 Emanuel, K.A. (1994). *Atmospheric convection.*: Oxford University Press on Demand

562 Eresmaa, N., Karppinen, A., Joffre, S.M., Rasanen, J., & Talvitie, H. (2006). Mixing height
563 determination by ceilometer. *Atmospheric Chemistry and Physics*, 6, 1485-1493

564 Fernald, F.G., 1984. Analysis of atmospheric lidar observations: some comments. *Appl. Opt.*
565 23, 652e653.

566 Flamant, C., Pelon, J., Flamant, P.H., & Durand, P. (1997). Lidar determination of the
567 entrainment zone thickness at the top of the unstable marine atmospheric boundary layer.
568 *Boundary-Layer Meteorology*, 83, 247-284

569 Gamage, N., & Hagelberg, C. (1993). Detection and Analysis of Microfronts and Associated
570 Coherent Events Using Localized Transforms. *Journal of the Atmospheric Sciences*, 50,
571 750-756

572 Gan, C.M., Wu, Y.H., Madhavan, B.L., Gross, B., & Moshary, F. (2011). Application of active
573 optical sensors to probe the vertical structure of the urban boundary layer and assess
574 anomalies in air quality model PM2.5 forecasts. *Atmospheric Environment*, 45,
575 6613-6621

576 Garratt, J.R. (1994). The Atmospheric Boundary-Layer - Review. *Earth-Science Reviews*, 37,
577 89-134

578 Geiss, A., Wiegner, M., Bonn, B., Schafer, K., Forkel, R., von Schneidmesser, E., Munkel, C.,
579 Chan, K.L., & Nothard, R. (2017). Mixing layer height as an indicator for urban air
580 quality? *Atmospheric Measurement Techniques*, 10, 2969-2988

581 Guo, J.P., Miao, Y.C., Zhang, Y., Liu, H., Li, Z.Q., Zhang, W.C., He, J., Lou, M.Y., Yan, Y.,
582 Bian, L.G., & Zhai, P. (2016). The climatology of planetary boundary layer height in
583 China derived from radiosonde and reanalysis data. *Atmospheric Chemistry and Physics*,
584 16, 13309-13319

585 Guo, J.P., Su, T.N., Li, Z.Q., Miao, Y.C., Li, J., Liu, H., Xu, H., Cribb, M., & Zhai, P.M.
586 (2017). Declining frequency of summertime local-scale precipitation over eastern China
587 from 1970 to 2010 and its potential link to aerosols. *Geophysical Research Letters*, 44,
588 5700-5708

589 Haeffelin, M., Angelini, F., Morille, Y., Martucci, G., Frey, S., Gobbi, G.P., Lolli, S., O'Dowd,
590 C.D., Sauvage, L., Xueref-Remy, I., Wastine, B., & Feist, D.G. (2012). Evaluation of
591 Mixing-Height Retrievals from Automatic Profiling Lidars and Ceilometers in View of
592 Future Integrated Networks in Europe. *Boundary-Layer Meteorology*, 143, 49-75

593 Hageli, P., Steyn, D.G., & Strawbridge, K.B. (2000). Spatial and temporal variability of
594 mixed-layer depth and entrainment zone thickness. *Boundary-Layer Meteorology*, 97,
595 47-71

596 Harrison, L., Michalsky, J., & Berndt, J. (1994). Automated Multifilter Rotating Shadow-Band
597 Radiometer - an Instrument for Optical Depth and Radiation Measurements. *Applied*
598 *Optics*, 33, 5118-5125

599 He, Q.S., Mao, J.T., Chen, J.Y., & Hu, Y.Y. (2006). Observational and modeling studies of
600 urban atmospheric boundary-layer height and its evolution mechanisms. *Atmospheric*
601 *Environment*, 40, 1064-1077

602 Holtslag, A.A. and Nieuwstadt, F.T. (1986). Scaling the atmospheric boundary layer.
603 *Boundary-Layer Meteorology*, 36(1-2), pp.201-209.

604 Hooper, W.P., & Eloranta, E.W. (1986). Lidar Measurements of Wind in the Planetary
605 Boundary-Layer - the Method, Accuracy and Results from Joint Measurements with
606 Radiosonde and Kytoon. *Journal of Climate and Applied Meteorology*, 25, 990-1001

607 Kaimal, J.C. and Finnigan, J.J. (1994). Atmospheric boundary layer flows: their structure and
608 measurement. Oxford university press.

609 Klett, J.D. (1985). Lidar Inversion with Variable Backscatter Extinction Ratios. *Applied*
610 *Optics*, 24, 1638-1643

611 Lee, K.H., Li, Z.Q., Cribb, M.C., Liu, J.J., Wang, L., Zheng, Y.F., Xia, X.G., Chen, H.B., & Li,
612 B. (2010). Aerosol optical depth measurements in eastern China and a new calibration
613 method. *Journal of Geophysical Research-Atmospheres*, 115

614 Lewis, J. R., Welton, E. J., Molod, A. M., & Joseph, E. (2013). Improved boundary layer
615 depth retrievals from MPLNET. *Journal of Geophysical Research: Atmospheres*, 118(17),
616 9870-9879.

617 Li, H., Yang, Y., Hu, X.M., Huang, Z.W., Wang, G.Y., Zhang, B.D., & Zhang, T.J. (2017a).
618 Evaluation of retrieval methods of daytime convective boundary layer height based on

619 lidar data. *Journal of Geophysical Research-Atmospheres*, 122, 4578-4593

620 Li, Z.Q., Guo, J.P., Ding, A.J., Liao, H., Liu, J.J., Sun, Y.L., Wang, T.J., Xue, H.W., Zhang,
621 H.S., & Zhu, B. (2017b). Aerosol and boundary-layer interactions and impact on air
622 quality. *National Science Review*, 4, 810-833

623 Lilly, D.K. (1968). Models of Cloud-Topped Mixed Layers under a Strong Inversion.
624 *Quarterly Journal of the Royal Meteorological Society*, 94, 292-&

625 Liu, B.M., Ma, Y.Y., Gong, W., Jian, Y., & Ming, Z. (2018). Two-wavelength Lidar inversion
626 algorithm for determining planetary boundary layer height. *Journal of Quantitative
627 Spectroscopy & Radiative Transfer*, 206, 117-124

628 Liu, S.Y., & Liang, X.Z. (2010). Observed Diurnal Cycle Climatology of Planetary Boundary
629 Layer Height. *Journal of Climate*, 23, 5790-5809

630 Liu, Z.Y., Hunt, W., Vaughan, M., Hostetler, C., McGill, M., Powell, K., Winker, D., & Hu,
631 Y.X. (2006). Estimating random errors due to shot noise in backscatter lidar observations.
632 *Applied Optics*, 45, 4437-4447

633 Lou, M., Guo, J., Wang, L., Xu, H., Chen, D., Miao, Y., ... & Li, J. (2019). On the relationship
634 between aerosol and boundary layer height in summer in China under different
635 thermodynamic conditions. *Earth and Space Science*. (In press)

636 Luo, T., Yuan, R., & Wang, Z. (2014). Lidar-based remote sensing of atmospheric boundary
637 layer height over land and ocean. *Atmospheric Measurement Techniques*, 7, 173-182

638 Mahrt, L. (1999). Stratified atmospheric boundary layers. *Boundary-Layer Meteorology*, 90(3),
639 pp.375-396.

640 Martin, C.L., Fitzjarrald, D., Garstang, M., Oliveira, A.P., Greco, S., & Browell, E. (1988).
641 Structure and Growth of the Mixing Layer over the Amazonian Rain-Forest. *Journal of
642 Geophysical Research-Atmospheres*, 93, 1361-1375

643 Matsui, T., Masunaga, H., Pielke, R.A., & Tao, W.K. (2004). Impact of aerosols and
644 atmospheric thermodynamics on cloud properties within the climate system. *Geophysical
645 Research Letters*, 31

646 Medeiros, B., Hall, A., & Stevens, B. (2005). What controls the mean depth of the PBL?
647 *Journal of Climate*, 18, 3157-3172

648 Melfi, S.H., Spinhirne, J.D., Chou, S.H., & Palm, S.P. (1985). Lidar Observations of Vertically

649 Organized Convection in the Planetary Boundary-Layer over the Ocean. *Journal of*
650 *Climate and Applied Meteorology*, 24, 806-821

651 Menut, L., Flamant, C., Pelon, J., & Flamant, P.H. (1999). Urban boundary-layer height
652 determination from lidar measurements over the Paris area. *Applied Optics*, 38, 945-954

653 Miao, Y.C., Guo, J.P., Liu, S.H., Wei, W., Zhang, G., Lin, Y.L., & Zhai, P.M. (2018). The
654 Climatology of Low-Level Jet in Beijing and Guangzhou, China. *Journal of Geophysical*
655 *Research-Atmospheres*, 123, 2816-2830

656 Monks, P.S., Granier, C., Fuzzi, S., Stohl, A., Williams, M.L., Akimoto, H., Amann, M.,
657 Baklanov, A., Baltensperger, U., Bey, I., Blake, N., Blake, R.S., Carslaw, K., Cooper,
658 O.R., Dentener, F., Fowler, D., Fragkou, E., Frost, G.J., Generoso, S., Ginoux, P., Grewe,
659 V., Guenther, A., Hansson, H.C., Henne, S., Hjorth, J., Hofzumahaus, A., Huntrieser, H.,
660 Isaksen, I.S.A., Jenkin, M.E., Kaiser, J., Kanakidou, M., Klimont, Z., Kulmala, M., Laj,
661 P., Lawrence, M.G., Lee, J.D., Liousse, C., Maione, M., McFiggans, G., Metzger, A.,
662 Mieville, A., Moussiopoulos, N., Orlando, J.J., O'Dowd, C.D., Palmer, P.I., Parrish, D.D.,
663 Petzold, A., Platt, U., Poschl, U., Prevo, A.S.H., Reeves, C.E., Reimann, S., Rudich, Y.,
664 Sellegri, K., Steinbrecher, R., Simpson, D., ten Brink, H., Theloke, J., van der Werf, G.R.,
665 Vautard, R., Vestreng, V., Vlachokostas, C., & von Glasow, R. (2009). Atmospheric
666 composition change - global and regional air quality. *Atmospheric Environment*, 43,
667 5268-5350

668 Morille, Y., Haefelin, M., Drobinski, P., & Pelon, J. (2007). STRAT: An automated algorithm
669 to retrieve the vertical structure of the atmosphere from single-channel lidar data. *Journal*
670 *of Atmospheric and Oceanic Technology*, 24, 761-775

671 Nieuwstadt, F.T.M. (1984). The Turbulent Structure of the Stable, Nocturnal Boundary-Layer.
672 *Journal of the Atmospheric Sciences*, 41, 2202-2216

673 Park, O.H., Seo, S.J., & Lee, S.H. (2001). Laboratory simulation of vertical plume dispersion
674 within a convective boundary layer - Research note. *Boundary-Layer Meteorology*, 99,
675 159-169

676 Platt, C.M., Young, S.A., Carswell, A.I., Pal, S.R., McCormick, M.P., Winker, D.M., Delguasta,
677 M., Stefanutti, L., Eberhard, W.L., Hardesty, M., Flamant, P.H., Valentin, R., Forgan, B.,
678 Gimmetstad, G.G., Jager, H., Khmelevtsov, S.S., Kolev, I., Kaprieolev, B., Lu, D.R.,

679 Sassen, K., Shamanaev, V.S., Uchino, O., Mizuno, Y., Wandinger, U., Weitkamp, C.,
680 Ansmann, A., & Wooldridge, C. (1994). The Experimental Cloud Lidar Pilot-Study
681 (Eclips) for Cloud-Radiation Research. *Bulletin of the American Meteorological Society*,
682 75, 1635-1654

683 Poltera, Y., Martucci, G., Coen, M.C., Hervo, M., Emmenegger, L., Henne, S., Brunner, D., &
684 Haefele, A. (2017). PathfinderTURB: an automatic boundary layer algorithm.
685 Development, validation and application to study the impact on in situ measurements at
686 the Jungfraujoch. *Atmospheric Chemistry and Physics*, 17, 10051-10070

687 Poulos, G.S., Blumen, W., Fritts, D.C., Lundquist, J.K., Sun, J., Burns, S.P., Nappo, C., Banta,
688 R., Newsom, R., Cuxart, J., Terradellas, E., Balsley, B., & Jensen, M. (2002). CASES-99:
689 A comprehensive investigation of the stable nocturnal boundary layer. *Bulletin of the*
690 *American Meteorological Society*, 83, 555-581

691 Sawyer, V., & Li, Z.Q. (2013). Detection, variations and intercomparison of the planetary
692 boundary layer depth from radiosonde, lidar and infrared spectrometer. *Atmospheric*
693 *Environment*, 79, 518-528

694 Seibert, P., Beyrich, F., Gryning, S.E., Joffre, S., Rasmussen, A., & Tercier, P. (2000). Review
695 and intercomparison of operational methods for the determination of the mixing height.
696 *Atmospheric Environment*, 34, 1001-1027

697 Seidel, D.J., Ao, C.O., & Li, K. (2010). Estimating climatological planetary boundary layer
698 heights from radiosonde observations: Comparison of methods and uncertainty analysis.
699 *Journal of Geophysical Research-Atmospheres*, 115

700 Sicard, M., Perez, C., Rocadenbosch, F., Baldasano, J.M., & Garcia-Vizcaino, D. (2006).
701 Mixed-layer depth determination in the Barcelona coastal area from regular lidar
702 measurements: Methods, results and limitations. *Boundary-Layer Meteorology*, 119,
703 135-157

704 Sinha, P.R., Manchanda, R.K., Kaskaoutis, D.G., Kumar, Y.B., Sreenivasan, S., 2013.
705 Seasonal variation of surface and vertical profile of aerosol properties over a tropical
706 urban station Hyderabad, India: VERTICAL AEROSOL CHARACTERISTICS. *J.*
707 *Geophys. Res. Atmos.* 118, 749e768.

708 Steyn, D.G., Baldi, M., & Hoff, R.M. (1999). The detection of mixed layer depth and

709 entrainment zone thickness from lidar backscatter profiles. *Journal of Atmospheric and*
710 *Oceanic Technology*, 16, 953-959

711 Stull, R.B. (1988). *An Introduction to Boundary Layer Meteorology*. Dordrecht: Springer
712 Netherlands

713 Su, T.N., Li, J., Li, C.C., Lau, A.K.H., Yang, D.W., & Shen, C.Y. (2017a). An intercomparison
714 of AOD-converted PM2.5 concentrations using different approaches for estimating
715 aerosol vertical distribution. *Atmospheric Environment*, 166, 531-542

716 Su, T.N., Li, J., Li, C.C., Xiang, P.Z., Lau, A.K.H., Guo, J.P., Yang, D.W., & Miao, Y.C.
717 (2017b). An intercomparison of long-term planetary boundary layer heights retrieved
718 from CALIPSO, ground-based lidar, and radiosonde measurements over Hong Kong.
719 *Journal of Geophysical Research-Atmospheres*, 122, 3929-3943

720 Su, T.N., Li, Z.Q., & Kahn, R. (2018). Relationships between the planetary boundary layer
721 height and surface pollutants derived from lidar observations over China: regional pattern
722 and influencing factors. *Atmospheric Chemistry and Physics*, 18, 15921-15935

723 Summa, D., Di Girolamo, P., Stelitano, D., & Cacciani, M. (2013). Characterization of the
724 planetary boundary layer height and structure by Raman lidar: comparison of different
725 approaches. *Atmospheric Measurement Techniques*, 6, 3515-3525

726 Tang, G., Zhu, X., Hu, B., Xin, J., Wang, L., Munkel, C., Mao, G., & Wang, Y. (2015). Impact
727 of emission controls on air quality in Beijing during APEC 2014: lidar ceilometer
728 observations. *Atmospheric Chemistry and Physics*, 15, 12667-12680

729 Tokinaga, H., Tanimoto, Y., Nonaka, M., Taguchi, B., Fukamachi, T., Xie, S.P., Nakamura, H.,
730 Watanabe, T., & Yasuda, I. (2006). Atmospheric sounding over the winter Kuroshio
731 Extension: Effect of surface stability on atmospheric boundary layer structure.
732 *Geophysical Research Letters*, 33

733 Tucker, S.C., Brewer, W.A., Banta, R.M., Senff, C.J., Sandberg, S.P., Law, D.C., Weickmann,
734 A.M., & Hardesty, R.M. (2009). Doppler Lidar Estimation of Mixing Height Using
735 Turbulence, Shear, and Aerosol Profiles. *Journal of Atmospheric and Oceanic Technology*,
736 26, 673-688

737 Wallace, J.M., & Hobbs, P.V. (2006). *Atmospheric science: an introductory survey*. Elsevier

738 Wang, Z., & Sassen, K. (2001). Cloud type and macrophysical property retrieval using

739 multiple remote sensors. *Journal of Applied Meteorology*, 40(10), 1665-1682.

740 Welton, E. J., Voss, K. J., Gordon, H. R., Maring, H., Smirnov, A., Holben, B., ... & Formenti,
741 P. (2000). Ground - based lidar measurements of aerosols during ACE - 2: Instrument
742 description, results, and comparisons with other ground - based and airborne
743 measurements. *Tellus B*, 52(2), 636-651.

744 Welton, E. J., J. R. Campbell, J. D. Spinhirne, and V. S. Scott (2001), Global monitoring of
745 clouds and aerosols using a network of micro-pulse lidarsystems, in *Lidar Remote
746 Sensing for Industry and Environmental Monitoring*, edited by U. N. Singh, T. Itabe, and
747 N. Sugimoto, Proc. SPIE, 4153, 151-158, Sendai, Japan.

748 Welton, E. J., & Campbell, J. R. (2002). Micropulse lidar signals: Uncertainty analysis, *J.
749 Atmos. Oceanic Technol.*, 19, 2089– 2094.

750 Whiteman, D.N., Demoz, B., Di Girolamo, P., Comer, J., Veselovskii, I., Evans, K., Wang, Z.,
751 Cadirola, M., Rush, K., Schwemmer, G., Gentry, B., Melfi, S.H., Mielke, B., Venable, D.,
752 & Van Hove, T. (2006). Raman lidar measurements during the International H2O Project.
753 Part I: Instrumentation and analysis techniques. *Journal of Atmospheric and Oceanic
754 Technology*, 23, 157-169

755 Yan, H.R., Li, Z.Q., Huang, J.P., Cribb, M., & Liu, J.J. (2014). Long-term aerosol-mediated
756 changes in cloud radiative forcing of deep clouds at the top and bottom of the atmosphere
757 over the Southern Great Plains. *Atmospheric Chemistry and Physics*, 14, 7113-7124

758 Yang, D.W., Li, C.C., Lau, A.K.H., & Li, Y. (2013). Long-term measurement of daytime
759 atmospheric mixing layer height over Hong Kong. *Journal of Geophysical
760 Research-Atmospheres*, 118, 2422-2433

761 Yang, T., Wang, Z.F., Zhang, W., Gbaguidi, A., Sugimoto, N., Wang, X.Q., Matsui, I., & Sun,
762 Y.L. (2017). Technical note: Boundary layer height determination from lidar for
763 improving air pollution episode modeling: development of new algorithm and evaluation.
764 *Atmospheric Chemistry and Physics*, 17, 6215-6225

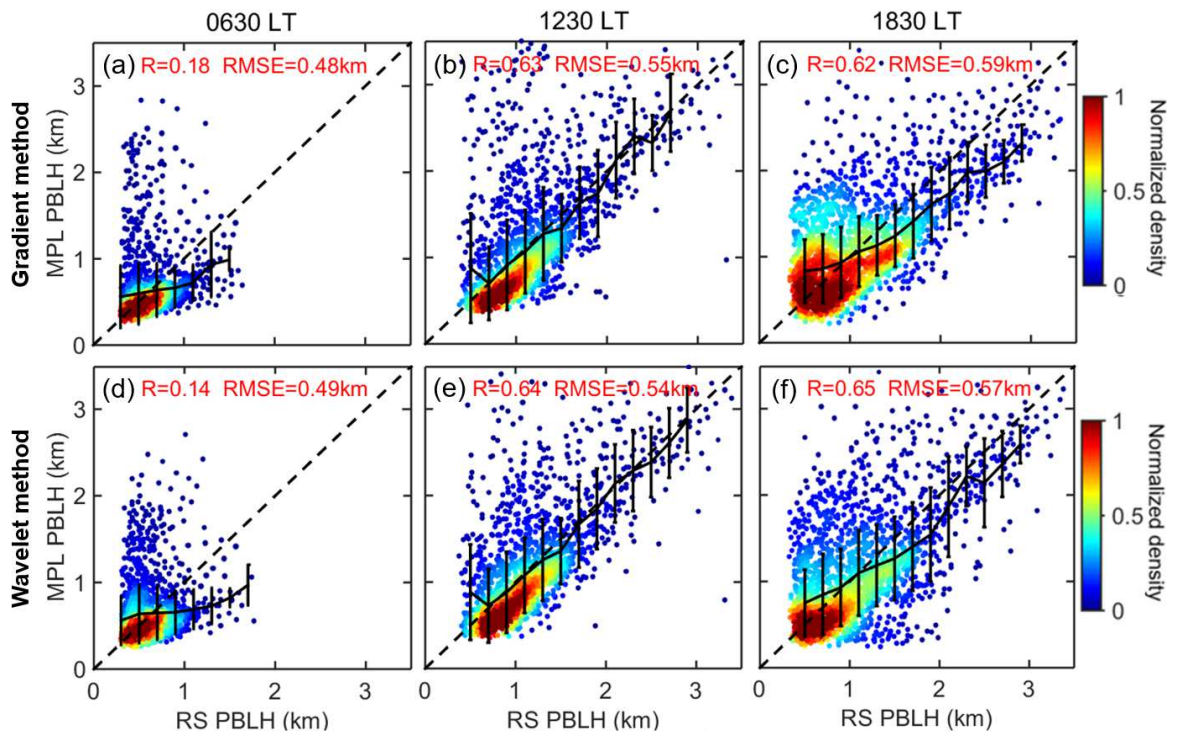
765 Zhao, C., Wang, Y., Wang, Q., Li, Z., Wang, Z., & Liu, D. (2014). A new cloud and aerosol
766 layer detection method based on micropulse lidar measurements. *Journal of Geophysical
767 Research: Atmospheres*, 119(11), 6788-6802.

768 Zhang, W., Guo, J., Miao, Y., Liu, H., Zhang, Y., Li, Z., & Zhai, P. (2016). Planetary boundary

769 layer height from CALIOP compared to radiosonde over China. *Atmospheric Chemistry*
770 *and Physics*, 16(15), 9951-9963.

771 Zhang, W.C., Guo, J.P., Miao, Y.C., Liu, H., Song, Y., Fang, Z., He, J., Lou, M.Y., Yan, Y., Li,
772 Y., & Zhai, P.M. (2018). On the Summertime Planetary Boundary Layer with Different
773 Thermodynamic Stability in China: A Radiosonde Perspective. *Journal of Climate*, 31,
774 1451-1465

775 **Figures**



776

777 **Fig. 1.** Comparisons between MPL PBLH (derived by the gradient method) and RS
778 PBLH for (a) 0630 LT, (b) 1230 LT, and (c) 1830 LT. Comparisons between MPL
779 PBLH (derived by the wavelet method) and RS PBLH for (d) 0630 LT, (e) 1230 LT,
780 and (f) 1830 LT. Correlation coefficients (R) and RMSE (root-mean-square error) are
781 given in each panel.

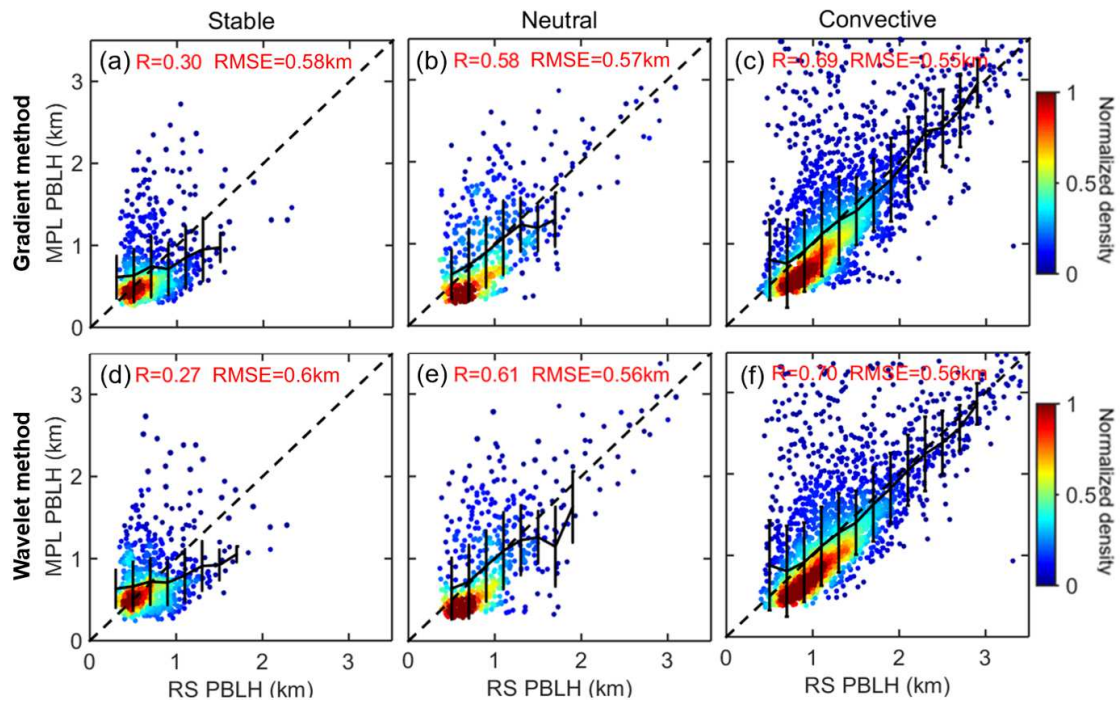
782

783

784

785

786



787

788 **Fig. 2.** Comparisons between MPL PBLH (derived by the gradient method) and RS
 789 PBLH for (a) stable (SBL), (b) neutral (NBL), and (c) convective (CBL) boundary
 790 layers during afternoon (1200-1900 LT). Comparisons between MPL PBLH (derived
 791 by the wavelet method) and RS PBLH for (d) SBL, (e) NBL, and (f) CBL.

792

793

794

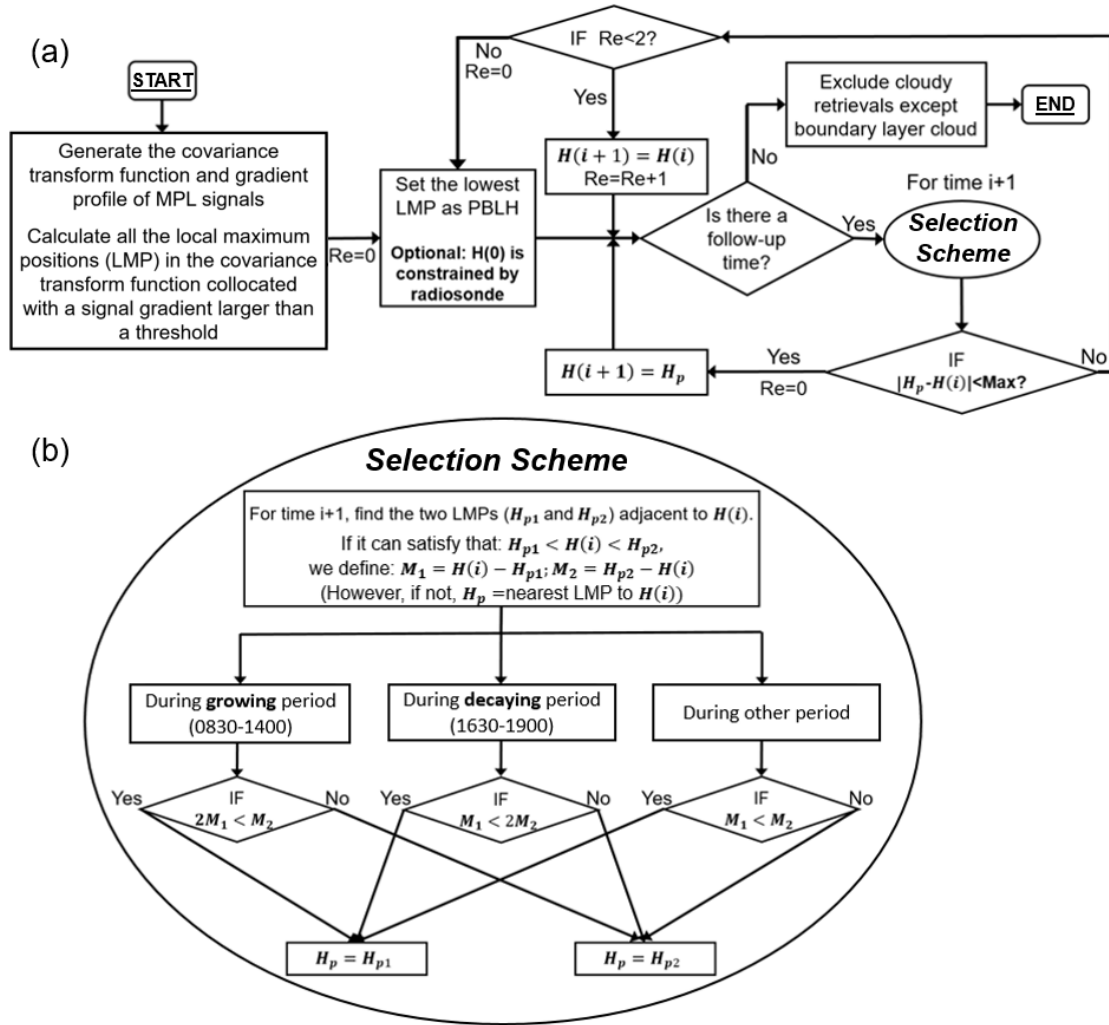
795

796

797

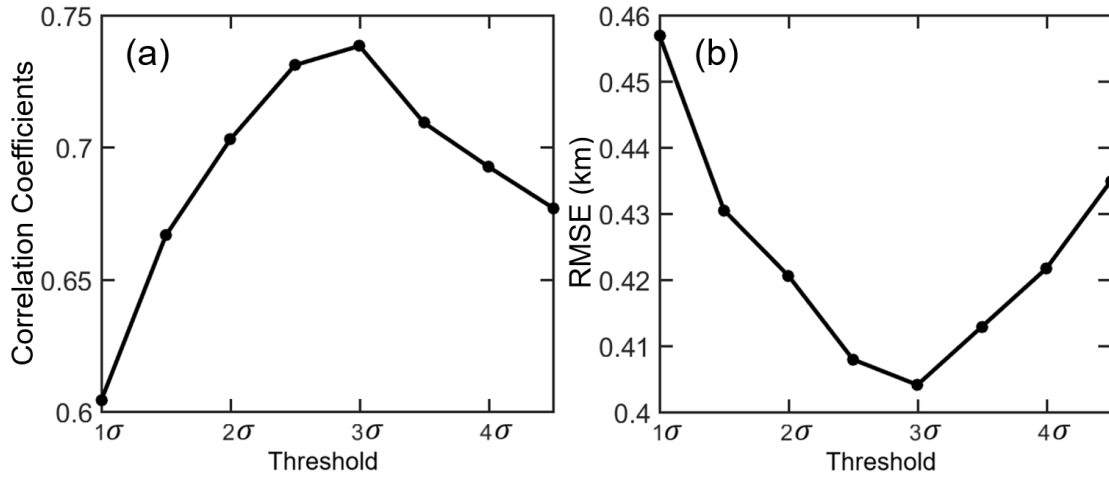
798

799



800

801 **Fig. 3.** (a) The overview schematic diagram of retrieving the PBLH by the DTDS. In
 802 this diagram, $H(i)$ indicates the retrieved PBLH for time i , and H_p indicates the
 803 potential PBLH position. The PBLH is retrieved at 10-minute intervals. Max
 804 indicate the maximum variation of PBLH allowed over 10-minutes, and is set as 0.2
 805 km in this study. (b) Schematic diagram of the selection scheme. The selection
 806 scheme is a process in the retrieval algorithm that describes how an appropriate local
 807 maximum position (LMP) as H_p is selected.



808

809 **Fig. 4.** Correlation coefficients and RMSE between the DTDS-derived PBLH and
 810 RS-derived PBLH under different threshold values during afternoon. The threshold
 811 value determines the algorithm LMP detection sensitivity. σ represents the shot noise
 812 induced by background light and dark current.

813

814

815

816

817

818

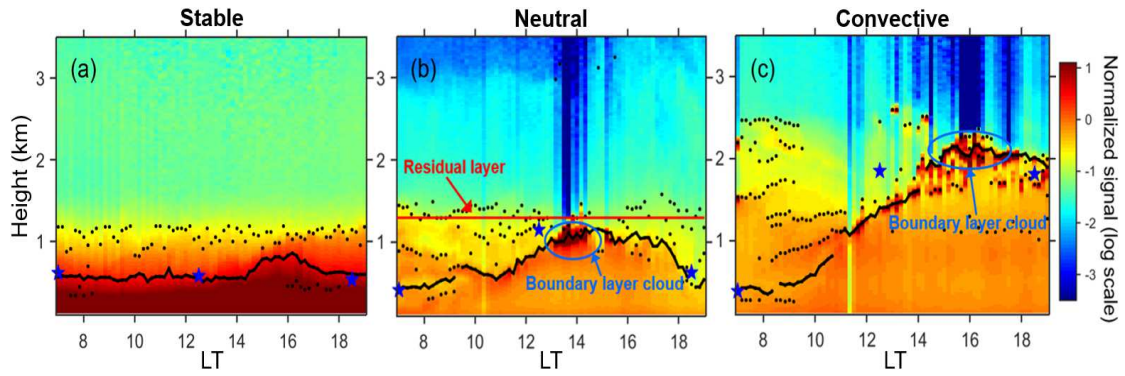
819

820

821

822

823



824

825 **Fig. 5.** Daily backscatter profiles for (a) SBL, (b) NBL, and (c) CBL cases.

826 Backscatter is presented as a normalized signal on a log-scale, in arbitrary units. Black

827 lines mark the PBLH retrieved from the DTDS. Black dots indicate the LMPs

828 identified in the backscatter profiles. The blue stars indicate the PBLH as derived

829 from RS.

830

831

832

833

834

835

836

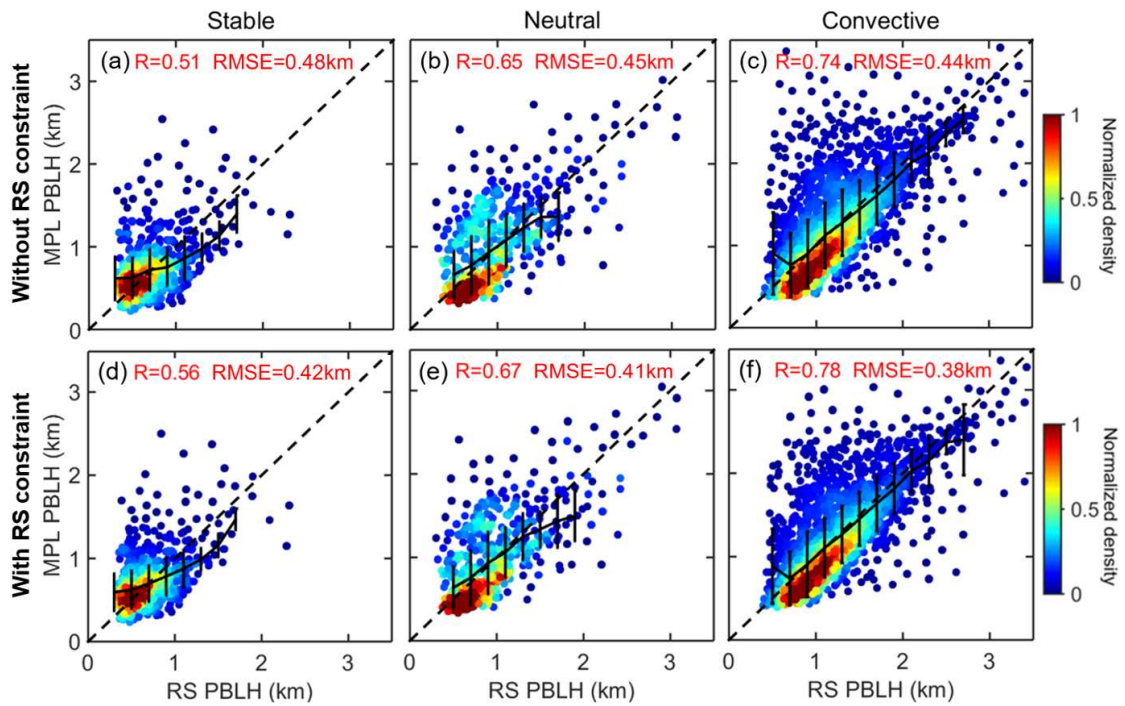
837

838

839

840

841



842

843 **Fig. 6.** Comparisons between afternoon PBLH derived from MPL and from RS under

844 different thermodynamic stability conditions. In (a, b, c), PBLH is calculated by

845 DTDS without the constraint of morning RS data. In (d, e, f), PBLH is calculated by

846 DTDS with a morning RS constraint.

847

848

849

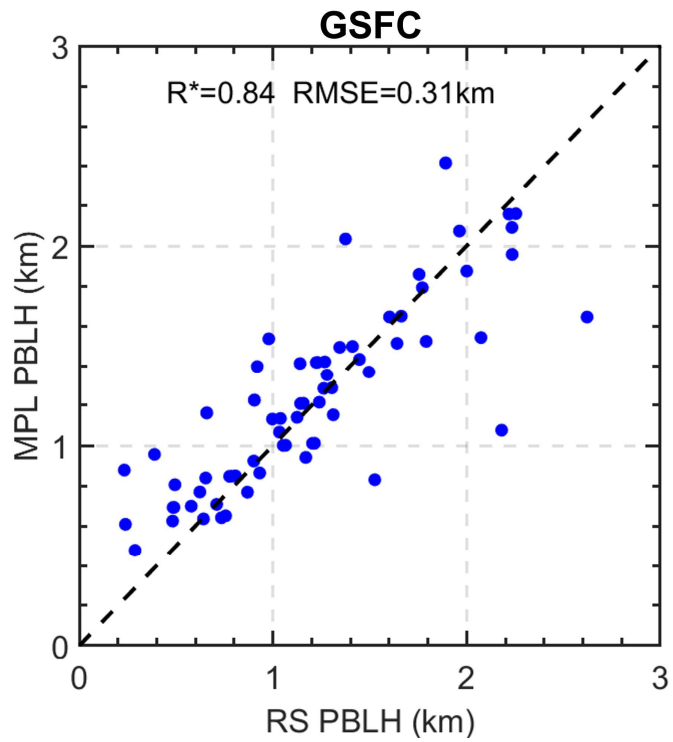
850

851

852

853

854



855

856 **Fig. 7.** Comparisons between afternoon PBLH derived from MPL and from RS at the
857 GSFC site. PBLH is calculated by DTDS with a morning RS constraint.

858

859

860

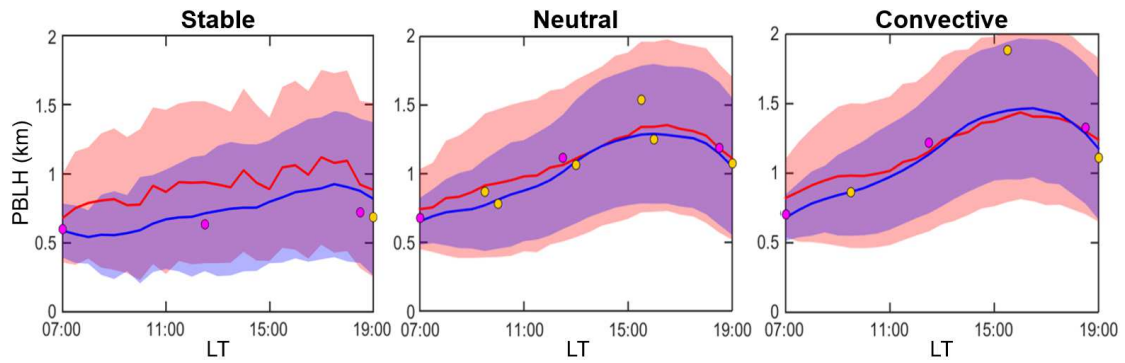
861

862

863

864

865



866

867 **Fig. 8.** Diurnal cycles of PBLH under (a) SBL, (b) NBL, and (c) CBL conditions,

868 which are determined based on RS at 1230LT. The blue lines indicate the PBLH

869 retrieved by the DTDS, and the red lines represent the averaged results derived from

870 the gradient and wavelet methods. The shaded areas show the standard deviation of

871 PBLH. Pink dots indicate the PBLH averaged from routine RS data, and yellow dots

872 indicate the PBLH averaged from RS with limited sampling.

873

874

875

876

877

878

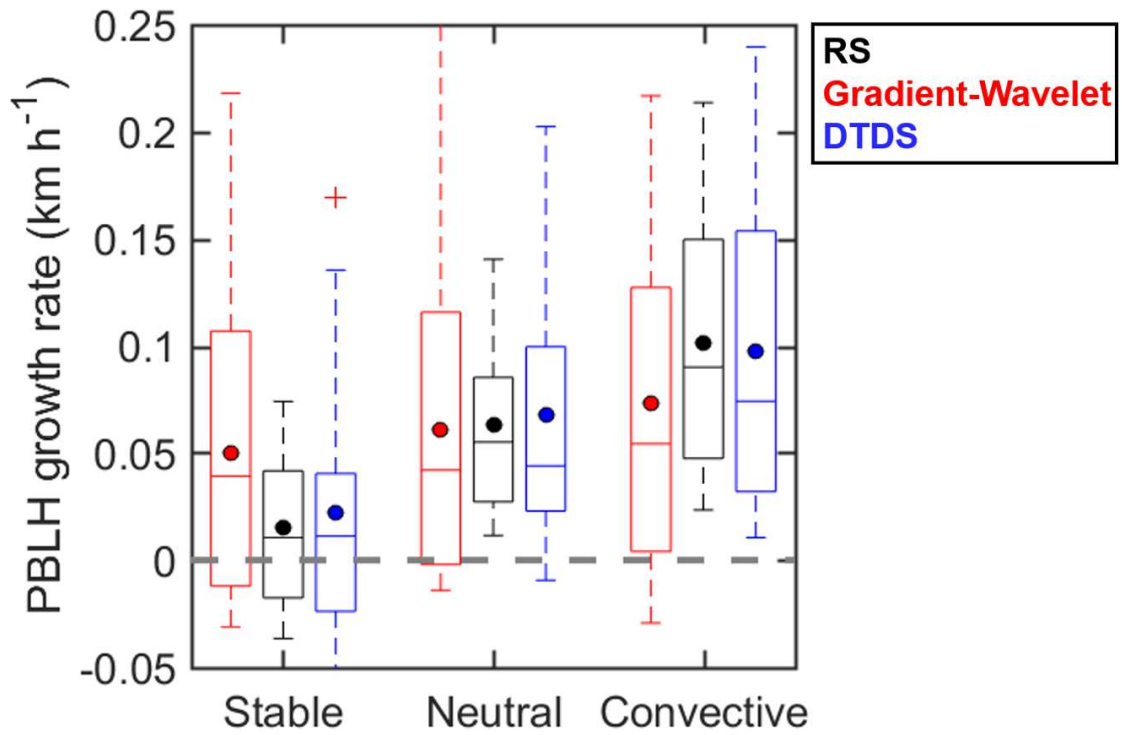
879

880

881

882

883



884

885 **Fig. 9.** Seasonal box-and-whisker plots showing 10th, 25th, 50th, 75th, and 90th
 886 percentile values of PBLH growth rate during 0700-1230 LT derived from
 887 Radiosonde (black), gradient and wavelet methods (red), and the DTDS from MPL
 888 (blue) under SBL, NBL, and CBL conditions.

889

890

891

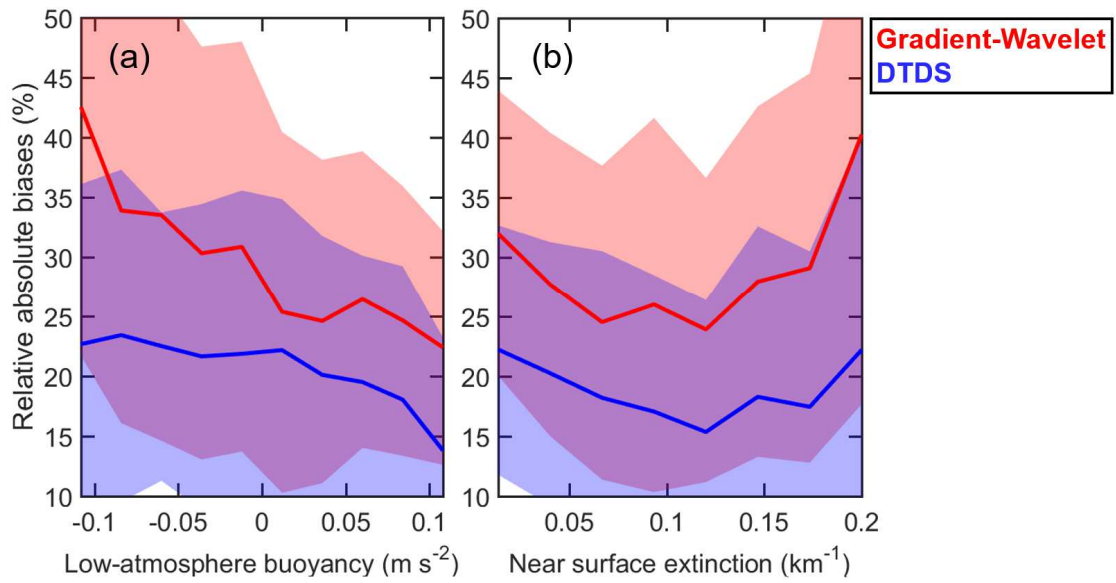
892

893

894

895

896



897

898 **Fig. 10.** Averaged relative absolute bias between afternoon PBLH derived from MPL
 899 and RS, for different (a) lower-atmosphere buoyancy and (b) near-surface aerosol
 900 extinctions. The blue line indicates the PBLH retrieved by the DTDS, and the red line
 901 represents the averaged results derived with the gradient and wavelet methods. The
 902 shaded areas indicate the standard deviations.

903